Article

Understanding Selectivity in CO_2 Hydrogenation to Methanol for MoP Nanoparticle Catalysts Using In Situ Techniques

Melis S. Duyar [1,2,3,*], Alessandro Gallo [1,2], Samuel K. Regli [4], Jonathan L. Snider [1,2], Joseph A. Singh [1,2], Eduardo Valle [1,2], Joshua McEnaney [1,2], Stacey F. Bent [1,2], Magnus Rønning [4] and Thomas F. Jaramillo [1,2,*]

[1] SUNCAT Center for Interface Science and Catalysis, Department of Chemical Engineering, Stanford University, 443 Via Ortega, Stanford, CA 94305, USA; agallo@slac.stanford.edu (A.G.); jonsnider.che@gmail.com (J.L.S.); jasingh@stanford.edu (J.A.S.); edvalle@stanford.edu (E.V.); dr.mcenaney@gmail.com (J.M.); sbent@stanford.edu (S.F.B.)

[2] SUNCAT Center for Interface Science and Catalysis, SLAC National Accelerator Laboratory, 2575 Sand Hill Road, Menlo Park, CA 94025, USA

[3] Department of Chemical and Process Engineering, University of Surrey, Guildford GU2 7XH, UK

[4] Department of Chemical Engineering, Norwegian University of Science and Technology, N-7491 Trondheim, Norway; samuel.k.regli@ntnu.no (S.K.R.); magnus.ronning@ntnu.no (M.R.)

* Correspondence: m.duyar@surrey.ac.uk (M.S.D.); jaramillo@stanford.edu (T.F.J.)

Abstract: Molybdenum phosphide (MoP) catalyzes the hydrogenation of CO, CO_2, and their mixtures to methanol, and it is investigated as a high-activity catalyst that overcomes deactivation issues (e.g., formate poisoning) faced by conventional transition metal catalysts. MoP as a new catalyst for hydrogenating CO_2 to methanol is particularly appealing for the use of CO_2 as chemical feedstock. Herein, we use a colloidal synthesis technique that connects the presence of MoP to the formation of methanol from CO_2, regardless of the support being used. By conducting a systematic support study, we see that zirconia (ZrO_2) has the striking ability to shift the selectivity towards methanol by increasing the rate of methanol conversion by two orders of magnitude compared to other supports, at a CO_2 conversion of 1.4% and methanol selectivity of 55.4%. In situ X-ray Absorption Spectroscopy (XAS) and in situ X-ray Diffraction (XRD) indicate that under reaction conditions the catalyst is pure MoP in a partially crystalline phase. Results from Diffuse Reflectance Infrared Fourier Transform Spectroscopy coupled with Temperature Programmed Surface Reaction (DRIFTS-TPSR) point towards a highly reactive monodentate formate intermediate stabilized by the strong interaction of MoP and ZrO_2. This study definitively shows that the presence of a MoP phase leads to methanol formation from CO_2, regardless of support and that the formate intermediate on MoP governs methanol formation rate.

Keywords: MoP; methanol synthesis; CO_2 hydrogenation; support effects; in situ characterization

1. Introduction

Carbon dioxide (CO_2) is a greenhouse gas produced globally as a byproduct of fossil fuel combustion and industrial activity [1]. Applications of CO_2 capture, utilization, and storage (CCUS) fall short of what is needed despite mounting evidence for the adverse effects of CO_2 emissions, such as climate change and ocean acidification [2–4]. There is a growing interest in developing advanced catalysts for CO_2 conversion to methanol (Equation (1)), in order to supply CO_2 as carbon feedstock to the broader chemical industry [5]. The reverse water gas shift reaction (Equation (2)) produces CO as a byproduct, leading to low methanol yields in CO_2 hydrogenation. Recent catalyst developments include high selectivity indium oxide catalysts [6–8], low pressure intermetallic catalysts [9–11] and metal phosphides facilitating flexible operation [12]. Herein, we present a strategy for synthesizing highly active molybdenum phosphide (MoP) catalysts for the hydrogenation of CO_2 to methanol, a product that is used as a fuel or as a chemical reagent in vast quantities,

with 110 million metric tons in annual global production in 2018 [13–16]. Introduction of CO_2 into the production of high value chemicals, such as methanol, can enable a future where CO_2 is leveraged as a globally distributed carbon building block to support society's demand for fuels and chemicals.

$$CO_2 + 3\,H_2 \rightarrow CH_3OH + H_2O \quad \Delta H^o_{298K} = -49.5 \text{ kJ mol}^{-1} \tag{1}$$

$$CO_2 + H_2 \leftrightarrow CO + H_2O \quad \Delta H^o_{298K} = 41.2 \text{ kJ mol}^{-1} \tag{2}$$
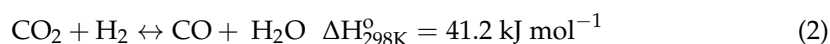
Commercial methanol synthesis mainly takes place over copper-zinc oxide (Cu/ZnO) catalysts which are optimized for operation with fossil fuel derived syngas ($CO/CO_2/H_2$) as reactant. When operating under CO_2 rich streams, these catalysts and transition metal surfaces, in general, suffer from kinetic limitations, due to a "poisoning" effect stemming from high coverages of the surface with CO_2 derived bidentate formate [12]. In our recent work [12], we demonstrated the robust activity of a supported MoP catalyst for the hydrogenation of CO, CO_2, and their mixtures to methanol, which is a unique result of its ability to circumvent scaling relations observed on transition metal catalysts. MoP avoids poisoning by bidentate formate because its crystal structure geometrically hinders bidentate adsorption, leading to a weaker monodentate adsorption of formate. This prompts a detailed exploration of the MoP system for CO_2 activation. In the present work, we adopt a colloidal synthesis technique reported previously for electrochemical hydrogen evolution reaction catalysts [17] to synthesize amorphous MoP particles of uniform size which are subsequently deposited on high surface area metal oxide supports. This allows us to perform a systematic study on support effects to explore the tunable activity of molybdenum phosphide nanoparticles for the thermochemical reduction of CO_2.

Sulfides [18–27], carbides [28–31], phosphides [12,32–35], and nitrides [36,37] of molybdenum have previously attracted interest for CO hydrogenation applications. Theoretical [38–40] and IR spectroscopy [41] studies have investigated CO binding and activation to elucidate the nature of active sites. CO_2 conversion has also been explored over molybdenum compounds, and these reports demonstrate greatly varying activity and selectivity patterns among catalysts based on molybdenum carbide [42–48], sulfide [49–51], phosphide [52,53], and nitride [54] catalysts. MoP has P terminated active sites, with electronic properties that can change depending on the adsorbent and local coordination of the P atom [52]. In some applications, this allows MoP to circumvent adsorbate scaling relations that impose limits on activity. In CO_2 hydrogenation to methanol, strong binding of O containing intermediates poses a limit to maximum attainable turnover frequency, and MoP has been shown in our previous work to circumvent this scaling limitation [55]. The flexible hybridization of the P atom on a MoP surface has been suggested as an active site which is not strictly governed by the scaling limitations affecting most catalysts [52]. This also makes MoP a highly tunable catalyst, allowing promotion effects to be exploited in favor of achieving both high selectivity and activity.

We recently employed an incipient wetness/temperature programmed reduction (TPR) method to synthesize MoP nanoparticles supported on silica, in a procedure modified from those reported in the hydrogenation and hydrotreating literature [32–34,56–58]. This synthesis resulted in catalysts with high activity towards methanol synthesis from hydrogenation of CO, CO_2, and their mixtures [12]. However, the TPR method relies on forming the MoP phase at a high temperature (700 °C) from an oxidic precursor. The formation of water from reduction of the oxidic precursor, along with the high temperature, leads to a high degree of sintering and formation of segregated MoP and MoO_x phases [12]. This has motivated the search for a synthesis technique that yields particles of uniform size on different supports, thus leading us to the colloidal method employed herein.

The source of P during transition metal phosphide synthesis has been shown to significantly influence the size and shape of the resulting particles [59,60]. In the present work, we use a colloidal synthesis method to form MoP nanoparticles, which are then impregnated onto reducible [61](ZrO_2, TiO_2, CeO_2, ZnO) and irreducible (Al_2O_3, SiO_2) metal oxide (MO)

supports. This technique eliminates the need for high temperatures to fully form the MoP phase. As metal phosphide particles are formed prior to impregnation onto these supports, these results provide for the first time a consistent comparison of activity of MoP for CO_2 hydrogenation, as well as provide insight on metal phosphide/support interactions for this reaction.

Herein, we report the CO_2 hydrogenation activity of MoP/MO catalysts prepared via a colloidal technique and use in situ X-ray Diffraction (XRD) and X-ray Absorption Spectroscopy (XAS) to show that this synthesis results in a mixture of crystalline and amorphous MoP under catalytic testing conditions. We present the vastly improved performance of MoP when supported on ZrO_2. MoP/ZrO_2 shows enhancement in activity and selectivity to methanol compared to all the other catalysts investigated in this study. To elucidate support effects, we take advantage of in situ Diffuse Reflectance Infrared Fourier Transform Spectroscopy (DRIFTS) to identify a highly reactive formate intermediate stabilized on MoP/ZrO_2, as well as to determine that it is responsible for the methanol synthesis activity enhancement.

2. Results and Discussion

2.1. Characterization of as-Synthesized Amorphous MoP Nanoparticles

A low temperature colloidal method was employed to synthesize amorphous MoP nanoparticles, which could be dispersed across different high surface area metal oxide supports to conduct a systematic study on the supported MoP catalyst system. The as-synthesized nanoparticles were dried and characterized using in situ XRD, in situ XAS, ex situ XPS, and ex situ transmission electron microscopy (TEM).

In situ XRD was performed during temperature programmed reduction (TPR) of the unsupported MoP nanoparticles to characterize crystalline phase evolution in the catalyst as a function of temperature under reducing conditions (Figure 1A). Room temperature measurements in hydrogen confirm the presence of only an amorphous phase in the as-synthesized nanoparticle powder, in accordance with prior work [17]. At 450 °C in pure hydrogen, XRD reveals a pure crystalline MoP phase, showing no crystalline impurities (Figure 1A). At 700 °C, MoP is still the only phase detected via XRD, showing sharper features (Figure 1A) and thus increased crystallinity and larger crystallite size (Figure 1B). In situ XRD, thus, shows that the degree of crystallinity can be controlled with reduction temperature. The 450 °C reduction treatment has previously been reported as the necessary treatment to remove ligands capping as-synthesized nanoparticles [17] and was chosen in this study as the temperature for pre-reduction of supported catalysts during reactor testing. This treatment was indeed found to be sufficient for ligand removal on supported catalysts, as shown by the representative data provided in Figure S1. Average particle size for the as-synthesized nanoparticles was also determined by TEM as 4 nm (Figure 1D), which is in alignment with prior work outlining the synthesis protocol [17]. This value cannot be compared to crystallite size measurements from XRD as, under room temperature conditions, the XRD does not show any peaks for the calculation of crystallite size.

The chemical structure of MoP nanoparticles was simultaneously tracked by in situ XAS at the Mo K-edge. X-ray Absorption Near Edge Spectroscopy (XANES) data at the Mo K-edge for the MoP nanoparticles during Temperature Programmed Reduction (TPR) in pure hydrogen are reported in Figure 2. The XANES spectra were collected from 50 °C up to 700 °C with a 10 °C/min ramp rate, and each spectrum was collected in a range of 20 °C. The sample was held at 450 °C and 700 °C for 3 scans before collecting the Extended X-ray Absorption Fine Structure (EXAFS) spectra. In order to better highlight the TPR trend, the difference spectra between each XANES collected during the TPR and the spectrum of the as-synthesized nanoparticles at room temperature is reported in Figure 2B. The corresponding first derivative of the XANES region is presented in Figure 2C.
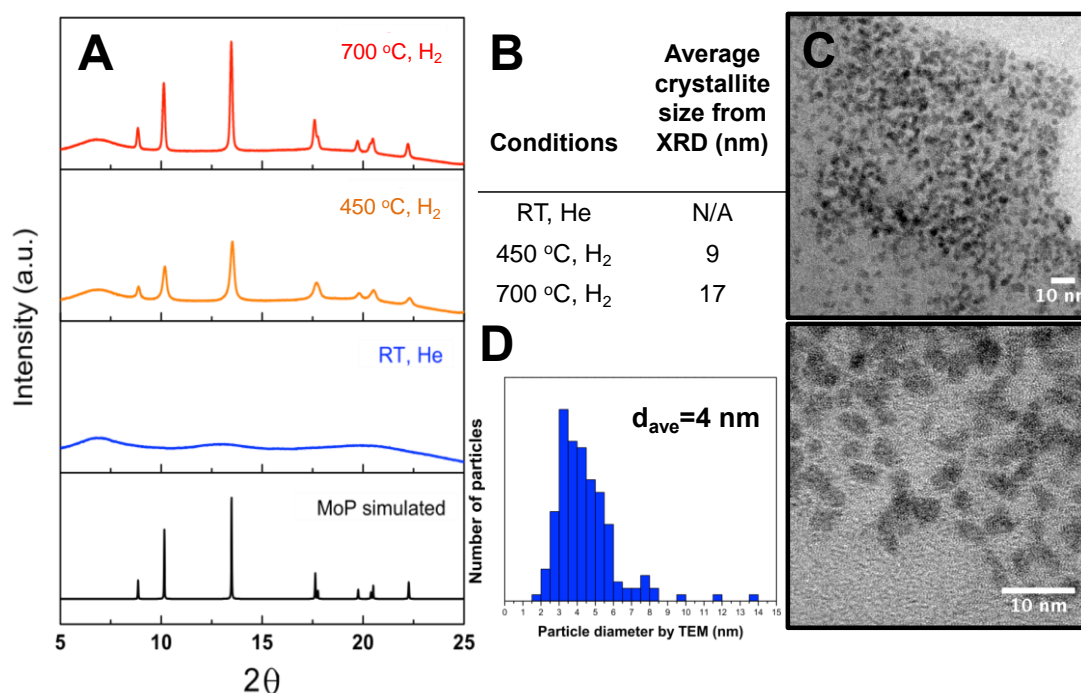
Figure 1. (**A**) In situ X-ray Diffraction (XRD) for unsupported molybdenum phosphide (MoP) nanoparticles during temperature programmed reduction. (**B**) Scherrer crystallite size analysis for unsupported MoP nanoparticles; (**C**) transmission electron microscopy (TEM) images for as-synthesized unsupported MoP nanoparticles; (**D**) particle size distribution from TEM using 163 particles.

Changes in the XANES region due to reduction and crystallization of the sample can be observed from the difference spectra (Figure 2B). An increase in intensity in the spectra develops during thermal treatment at onset of the absorption edge, with maximum at 20,009 eV and a shoulder at 20,003 eV, together with two other features in the main edge region, a broad maximum at 20,026 eV and minimum at 20,017 eV (Figure 2B). Comparing the difference spectra at temperatures exceeding 450 °C with the difference between crystalline MoP and with the as-synthesized colloidal nanoparticles (Figure S2), it is possible to conclude that the activation process is nearly complete below 450 °C and minimal changes develop at higher temperatures. The first derivative of the XANES region is particularly useful in understanding the reduction process and the nature of the as-synthesized nanoparticles. Clearly, the first derivative of the XANES of the colloidal nanoparticles presents two features characteristic of crystalline MoP at 20,001 eV and 20,007 eV, along with a peak at 20,015 eV due to the presence of oxidized Mo (Figure S3), evidencing the formation of amorphous metal phosphide upon colloidal synthesis, along with the presence of oxidized Mo. The latter species starts to reduce above 150 °C, as the feature at 20,015 eV in the first derivative decreases, while proper crystallization occurs rapidly above 350 °C when the feature at 20,013 eV and 20,019 eV, that are characteristic of crystalline MoP (Figure S3), appear and gain in intensity. Above 450 °C, well-formed MoP nanoparticles are present, and the XANES region does not significantly evolve further with the temperature increase (Figure 2C).
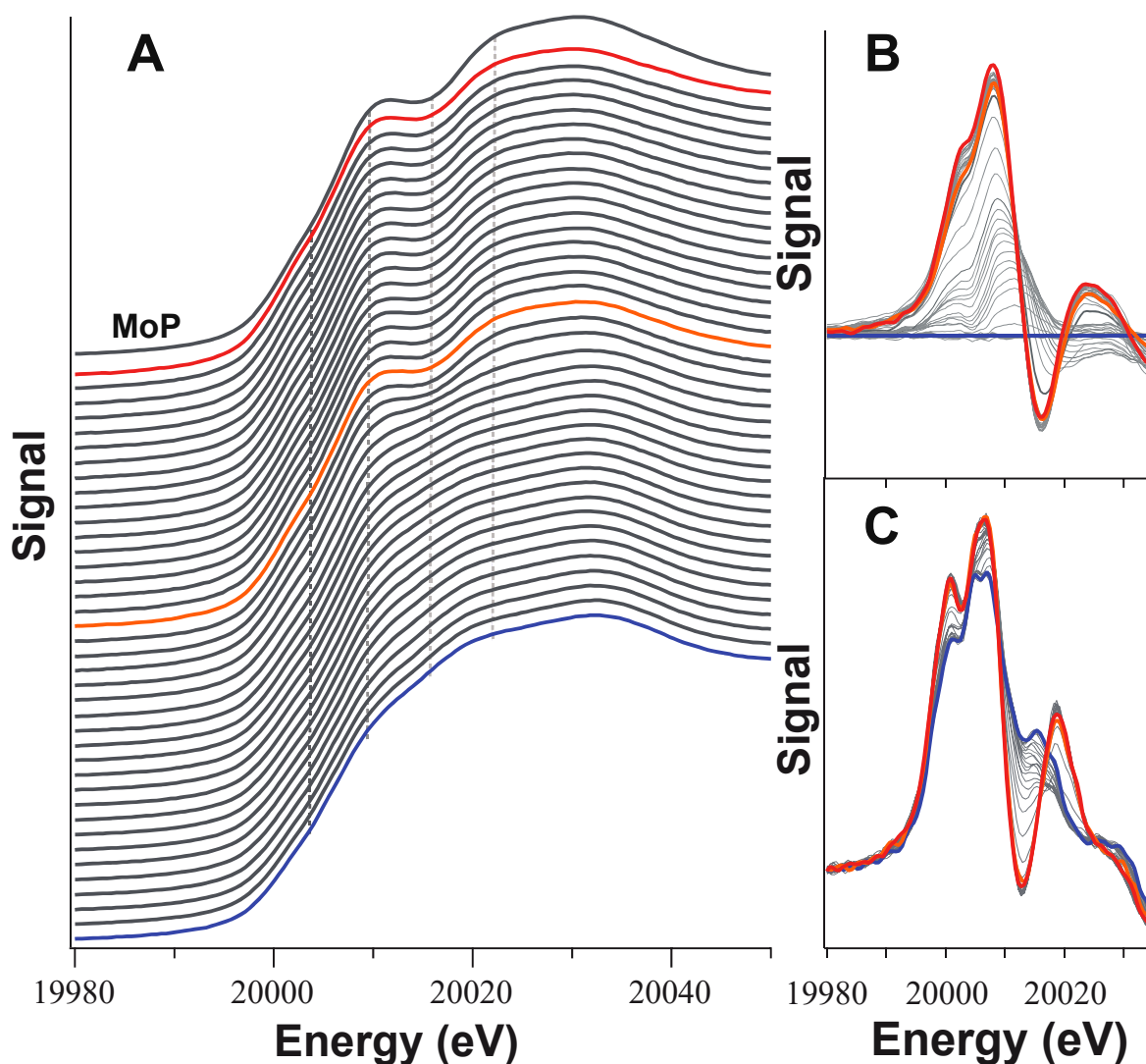
Figure 2. X-ray Absorption Near Edge (XANES) region at Mo K-edge during temperature programmed reduction (TPR). (**A**) XANES region: The XANES spectra were collected from 50 °C up to 700 °C with a 10 °C/min ramp rate and each spectrum was collected in a range of 20 °C; (**B**) series of difference spectra between each XANES collected during the TPR and the spectrum of the as-synthesized nanoparticles. (**C**) First-derivative of the XANES spectra collected during TPR. Blue line: 50 °C; orange line: 450 °C; red curve: 700 °C.

EXAFS analysis also confirms XANES-TPR analysis results. The Fourier Transform (FT) of the EXAFS signal for the as-synthesized MoP nanoparticles (NPs) presents a complex first shell that clearly results in a main peak at 2 Å (Figure 3A; not-phase-shift corrected FT), ascribable to a Mo-P bond, and a shoulder at shorter distances due to oxidized Mo, as quantitatively shown in Table S1. The Mo-P distance of 2.43 Å and its coordination number of 5 are similar to the crystalline MoP phase; however, the large Debye-Waller factor (0.013 Å^2) indicates that the nanoparticles are amorphous. This is also supported by the absence of the longer distance shells for Mo-Mo as shown in the EXAFS of the sample treated at high temperature. At 450 °C, the contributions for the oxidized Mo are no longer pronounced, and a distinct peak due to Mo-Mo scattering path appears at 3 Å (Figure 3A; not-phase-shift corrected FT), confirming the partial formation of crystalline MoP [57]. The quantitative fitting results show a Mo-P bond at 2.44 Å and a distance Mo-Mo of 3.21 Å, comparable to the values for crystalline MoP. The coordination number (CN = 5.3) and bond distance for the Mo-P shell at 450 °C are similar to those revealed at room temperature and are similar to crystalline MoP, while the coordination number

for the Mo-Mo scattering path is significantly smaller compared to the MoP standards (CN = 3 vs. 8), as is the intensity of the Mo-Mo shell center at 4 Å (not-phase-shift corrected FT). We can conclude that the nanoparticles still present a significant amorphous character at 450 °C. Upon increasing the temperature to 700 °C, no significant changes in the EXAFS are observed. Similar conclusions can also be drawn when the nanoparticles were dropcast onto silica support (Figure S4)
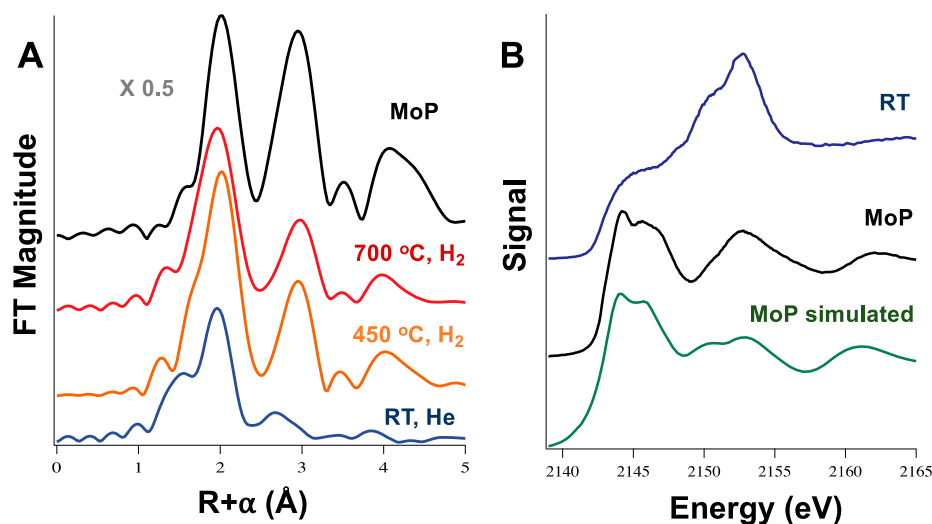

Figure 3. (**A**) Fourier Transform of the Extended X-ray Absorption Fine Structure (EXAFS) oscillation for the Mo K-edge collected in situ. Bottom to top: as-synthesized colloidal MoP nanoparticles at room temperature (RT) in He; MoP nanoparticles at 450 °C in H_2; MoP NPs at 700 °C in H_2. (**B**) XANES spectra at P K-edge (air-exposed samples). Bottom to top: Simulated XANES at P k-edge for crystalline MoP; crystalline MoP; as-synthesized MoP colloidal NPs.

The XANES spectrum for P K-edge of the as-synthesized MoP NPs is reported in Figure 3B, together with the experimental spectra for MoP standard and simulated MoP. The XANES of the MoP standard is well represented by the simulation using its common crystallographic structure, confirming its phase purity and absence of other prominent crystalline and amorphous components. It is clear that several P species in different oxidation states are present after colloidal synthesis. The partial formation of metal phosphide is evidenced by the low energy absorption peak centered 2145 Ev [62]. Its featureless character compared to crystalline MoP confirms the amorphous nature of the as-synthesized nanoparticles [12,35,57]. Other absorption peaks, characteristic of P in higher oxidation states, are also visible in the spectrum. In particular, the feature at 2150 eV (P^{+1}) is linked to pristine or partially decomposed residual trioctyl phosphine (TOP) ligand from synthesis, and the peak at 2152 eV shows the formation phosphate upon air-exposure [63].

In previous studies, we revealed how the formation of MoP phase at high temperature is deeply influenced by the nature of the support (amorphous silica, SBA-15, carbon) and promoters when we started the thermal synthesis of MoP from inorganic precursors dispersed onto the support [12,35]. In the case of colloidal synthesis, the formation of a crystalline MoP phase also requires a high temperature treatment under a hydrogen atmosphere. The nature of these colloidally prepared MoP nanoparticles is significantly different at all temperatures compared to the ones previously reported [12,35] since the post-synthesis thermal treatment results in a lower degree of crystallinity (likely due to the much smaller particle size of the starting MoP), as evidenced by the small coordination number for the first Mo-Mo scattering path and the low intensity of the longer contributions in the EXAFS. During the thermal activation, two main processes occur: partial crystallization of the amorphous phosphide formed during colloidal synthesis and reduction of residual oxidized Mo (formed during air-exposure) with concomitant decomposition of the residual

TOP ligand (from synthesis) that promotes the formation of a nanosized MoP phase that is complete by 450 °C.

2.2. Characterization of Supported MoP Nanoparticles

To prepare catalysts for CO_2 hydrogenation, the amorphous MoP nanoparticles were impregnated on various supports. Elemental analysis was performed on the supported catalysts after activation in hydrogen at 450 °C using Inductively Coupled Plasma-Mass Spectrometry (ICP-MS) to determine their molybdenum and phosphorus content (Table S2). TEM images obtained on reduced catalysts (Figure 4) indicate that the synthesis on silica, titania, and alumina yields well-dispersed nanoparticles. On ceria and zinc oxide, large clusters of MoP were observed, likely due to weaker interactions with the pores of those particular supports. For the case of zirconia, due to the low loading, as well as the low contrast of the Mo and Zr atoms in TEM, distinct MoP nanoparticles could not be observed (Figure 4), consistent with prior reports [64]. The variation in nanoparticle loading can be explained by losses during the particle recovery procedure, as well as differences in surface area of the support. The spatial distribution of particles (inside pores vs. outside) is affected by both the pore size distribution, as well as surface charge [35]. These parameters are identified as the subject of subsequent optimization studies.
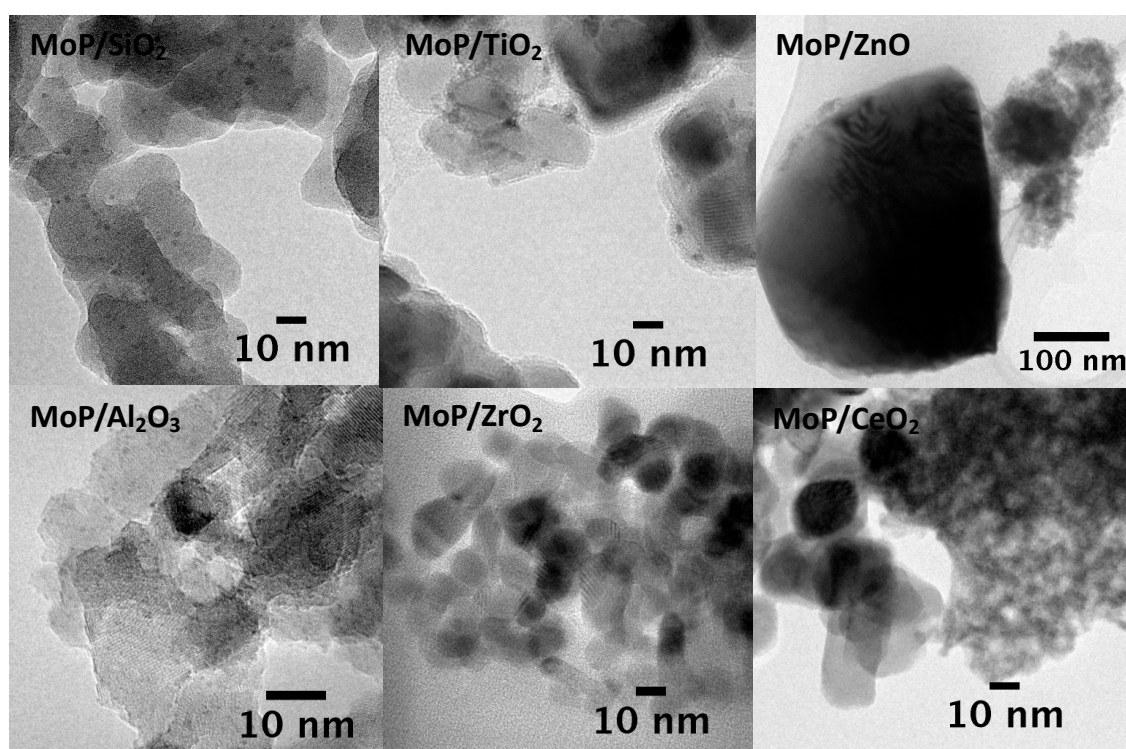

Figure 4. TEM image showing nanoparticles supported on SiO_2, TiO_2, ZnO, Al_2O_3, ZrO_2, and CeO_2. All catalysts underwent a reduction treatment in pure hydrogen at 450 °C for 1 h prior to imaging.

2.3. CO$_2$ Hydrogenation: Systematic Support Study

Catalytic activity was evaluated under CO_2 hydrogenation conditions at 40 bar. Figure 5A displays the CO selectivity, as well as rate of methanol formation normalized with respect to Mo loading on the different supports. The CO_2 conversion and other relevant activity metrics of the catalysts are provided in Table S3. All catalysts are active for reverse water gas shift (producing CO) and methanol synthesis. CO-free full product distributions are presented in Figure 5B, which shows that, regardless of support, a phase pure MoP catalyst synthesizes methanol as the dominant product. This is in line with prior theoretical and experimental work on MoP catalysts prepared via incipient wetness

impregnation, showing that the formation of the MoP phase is the most important factor affecting methanol synthesis activity in CO_2 and CO hydrogenation conditions [12]. While the commonly employed temperature programmed reduction method for the synthesis of transition metal phosphides yields mixtures of phosphide, oxide, and phosphate phases, the colloidal technique presented herein results in the stabilization of exclusively the MoP phase, allowing us to elucidate support effects with more clarity.
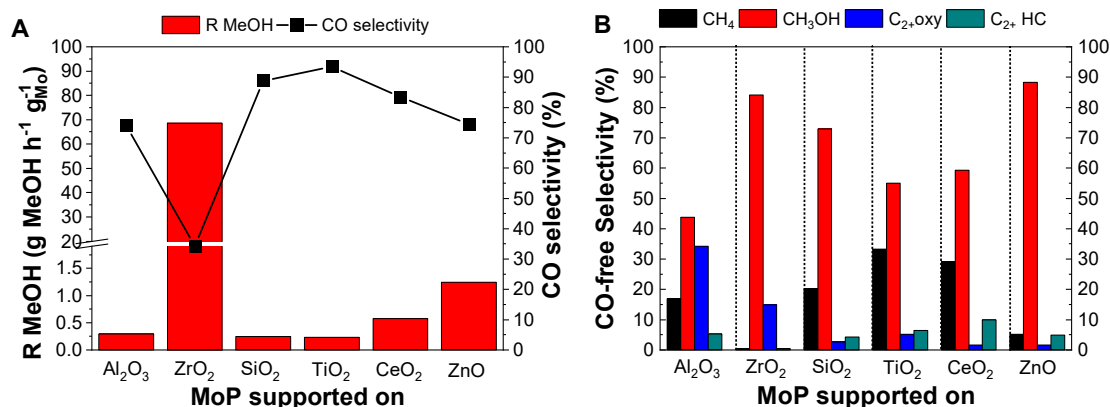

Figure 5. (**A**) CO selectivity and normalized activity of supported MoP catalysts (**B**) CO-free selectivity of supported MoP catalysts. Test conditions: CO_2 hydrogenation, 40 bar, 250 °C, H_2/CO_2 = 3, Conversion = 0.3–1.8%.

ZrO_2 supported MoP nanoparticle catalyst shows exceptional normalized activity for methanol synthesis with suppressed CO formation (Figure 5A). The overall CO_2 conversion on MoP/ZrO_2 is also among the highest (1.42%, from Table S3), despite the low loading of Mo (0.05%, from Table S2). Selectivity to methanol is 55.4%, which is near equilibrium selectivity for the testing conditions employed [65] (Figure 5B). The ZrO_2 support under identical test conditions shows minimal activity for CO_2 reduction (<200 ppm CO and methanol formation as shown in Figure S7), indicating a synergistic effect between ZrO_2 and MoP leading to superior activity.

While the mechanisms proposed are different for CO_2 hydrogenation on Cu and MoP, a significant promotion effect associated with ZrO_2 support has been observed previously on Cu catalysts, as well [61,66]. For Cu/ZrO_2, the metal support interface has been proposed in some studies to stabilize a highly reactive formate intermediate in methanol formation [66], as well as in other works, suggested to unlock a new mechanism for methanol synthesis that proceeds via CO_2 reduction to CO and subsequent hydrogenation to methanol via a carboxyl intermediate [61]. Additionally, on Cu catalysts, ZrO_2 has been reported to play a multitude of roles in methanol synthesis [67,68], including facilitating water desorption [69,70], modifying CO_2 and H_2 activation [71–73], and improving active site distribution [74] to name a few. Hence, a deeper look into the MoP/ZrO_2 system is motivated with the aim of uncovering the underlying reasons for the promotion effects, which have previously not been studied for this catalyst.

Table 1 compares the conversion and selectivity for MoP/ZrO_2 in the present work with previously reported CeO_2 promoted MoP catalyst, as well as the commercial $Cu/ZnO/Al_2O_3$ and zirconia promoted Cu catalysts. Additionally, recently reported promising catalysts for CO_2 hydrogenation to methanol, such as $Pd-In_2O_3$ and $ZnO-ZrO_2$ solid solution, are included in Table 1. It can be seen that, from a conversion and selectivity perspective, MoP/ZrO_2 is competitive with our previously best performing CeO_2 promoted MoP catalyst prepared via the temperature programmed reduction method, despite the low loading of MoP in MoP/ZrO_2. The superior activity resulting from the $MoP-ZrO_2$ synergy suggests that, by increasing the number of active sites, it will be possible to develop a commercially viable system, at higher loadings of MoP on ZrO_2. Based on Table 1, another

interesting avenue of research will be to explore $ZnO-ZrO_2$ solid solution as a support for MoP, to boost the activity even further.

Table 1. Comparative performance of MoP/ZrO_2 with other reported catalysts for methanol synthesis from CO_2.

Catalyst	Temperature (°C)	Pressure (bar)	Space Velocity $(mL\ g^{-1}\ h^{-1})$	H_2/CO_2	Conversion (%)	Methanol Selectivity (%)	Reference
MoP/ZrO_2	250	40	19,200	3	1.4	55.4	This work
CeO_2 MoP K/SiO_2	230	31	19,200	3	<2	76	[12]
Commercial $Cu/ZnO/Al_2O_3$	230	31	19,200	3	<2	72	[12]
Cu/ZrO_2	230	25	1565	3	2.7	20	[66]
$Pd-In_2O_3$ CP	280	50	48,000	4	9.7	78	[7]
$ZnO-ZrO_2$ solid solution	315	50	24,000	4	10	91	[75]

2.4. Identification of Surface Species during CO_2 Hydrogenation

In order to identify surface bound species that can provide insights into the synergistic effect of ZrO_2 and MoP nanoparticles for methanol synthesis, we investigated surface adsorbates during CO_2 hydrogenation (8.8 bar) on the MoP/ZrO_2 catalyst using DRIFTS coupled with Temperature Programmed Surface Reaction (DRIFTS-TPSR). Figure 6 displays the surface species in the CO stretch region during CO_2 hydrogenation at increasing temperatures (50–250 °C) over MoP/ZrO_2 and ZrO_2. The surface species observed and their assignments to the spectra are presented in Table 2. From Figure 6, it is apparent that the MoP/ZrO_2 stabilizes more surface species during this reaction compared to the crystalline MoP supported on SiO_2 studied under similar reaction-DRIFTS conditions. While the crystalline MoP reported previously showed only 2 distinct bands in this region attributed to monodentate formate, the complex spectra of MoP/ZrO_2 suggests the stabilization of a variety of carbonate and formate species (Table 2), to be discussed below.
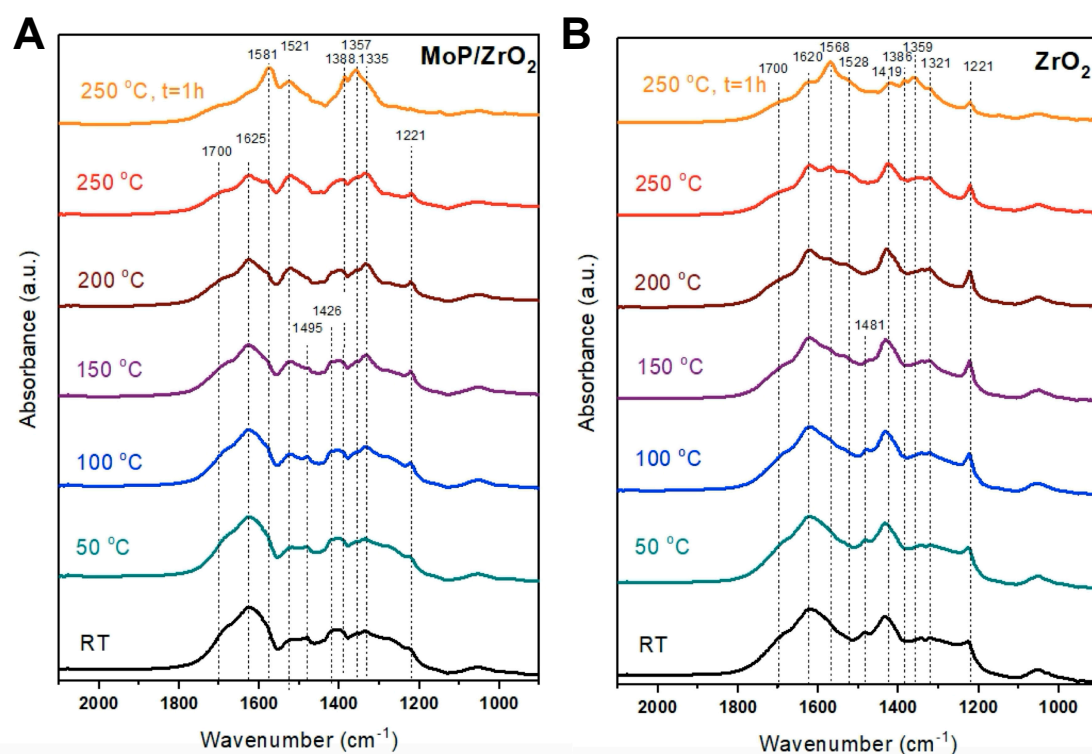

Figure 6. Diffuse Reflectance Infrared Fourier Transform Spectroscopy-Temperature Programmed Surface Reaction (DRIFTS-TPSR) of MoP/ZrO_2 (**A**) and ZrO_2 (**B**) at 8.8 bar to 250 °C. Both tests performed after reduction at 450 °C in hydrogen.

Based on previous reports of CO_2 hydrogenation-DRIFTS on ZrO_2 supported catalysts, several of these formate and carbonates have been identified in Table 2. The large number of peaks present and their close proximity prevent the definitive assignment of adsorption geometries, particularly for the formates. It can be seen from both Figure 6 and Table 2 that ZrO_2 alone stabilizes bridged carbonate (1528, 1331 cm^{-1}) and bicarbonate (1620, 1419, 1221 cm^{-1}) species, which are also present on MoP/ZrO_2 and are hence attributed to species adsorbed on the support [12]. At room temperature, both samples also show a broad peak centered at 1057 cm^{-1} (ZrO_2) and 1054 cm^{-1} (MoP/ZrO_2). This broad peak has been assigned to monodentate carbonate [12]. While methoxy species on ZrO_2 can also show a peak in this region, these are ruled out by the absence of the asymmetric and symmetric CH_3 stretching (($\nu_{a,}(CH_3)$, $\nu_{s,}(CH_3)$)) bands [76] which appear at much higher temperatures (2929, 2828 cm^{-1} for ZrO_2 and 2940, 2824 cm^{-1} for MoP/ZrO_2 at 250 °C), as shown in Figures S8–S10. The role of methoxy is difficult to discern from these experiments, as it is known that methanol is chemisorbed on ZrO_2 in the form of methoxy [77], but methoxy can also play a role in the catalytic mechanism [76].

The asymmetric and symmetric CO_2 stretching modes ($\nu_{a,}(CO_2)$, $\nu_{s,}(CO_2)$)of formate are identified at 1568 and 1359 cm^{-1} on the bare ZrO_2 support, consistent with prior reports at similar conditions [66]. The prominent formate bands on MoP/ZrO_2 are further apart from each other, observed at 1581 and 1357 cm^{-1}, indicating a weaker interaction of formate with MoP/ZrO_2, compared to ZrO_2 alone. These bands are ascribed to monodentate formate on MoP. The separation ($\Delta\nu$) of $\nu_{a,}(CO_2)$ and $\nu_{s,}(CO_2)$ can be used to distinguish between the different formate adsorption geometries, with $\Delta\nu$ values greater than that for the free formate ion (200–220 cm^{-1}) being ascribed to monodentate species and those of decreasing separation being ascribed to more strongly bound bridged bidentate or bidentate species [78–84]. A separation of 209 cm^{-1} is observed for the formate bands on bare ZrO_2, whereas a separation of 224 cm^{-1} is observed on MoP/ZrO_2. This value is less than the separation we previously observed for monodentate formate on silica supported MoP (247 cm^{-1}) [12], but it is still within range of reported values for monodentate formate. The formate binding is clearly stronger on MoP/ZrO_2 compared to crystalline MoP on silica in our earlier work. Both the partly amorphous nature of the MoP nanoparticles in this study and their strong interaction with ZrO_2 can be responsible for the stronger interaction of this key intermediate with the catalyst surface, yet the significantly crystalline nature of the MoP nanoparticles under these conditions (as observed by in situ XRD) indicates that this is likely an effect stemming from the strong interaction of zirconia with MoP. We know from previous investigations [12] that strengthening formate binding too much (such as in the case of b-HCOO⁻) results in a kinetic deactivation effect. Hence, it is likely that there is an optimum binding energy for monodentate formate which can be identified with further systematic studies. Density functional theory (DFT) and microkinetic modeling, together with controlled synthesis (e.g., varying nanoparticle size on ZrO_2) and in situ/*operando* DRIFTS, will be very informative in this regard. Another notable finding from TPSR is that carbonate species on the support transform to formate on MoP/ZrO_2 after 1 h on stream at 250 °C (Figure 6A). Hence, the role of zirconia support is seen to be twofold: The zirconia support stabilizes carbonates, which are subsequently transformed to methanol via a formate route on MoP, while also modifying MoP to stabilize a more reactive formate (Figure 7).

It was shown in our previous work through DFT, DRIFTS, XAS, and activity testing that underphosphided or metal terminated regions on MoP/SiO_2 behave similarly to metallic Mo, which is responsible for the formation of CO and a small amount of hydrocarbons during CO_2 hydrogenation [12]. Based on our earlier DFT and DRIFTS findings, monodentate formate on phosphorous terminated MoP sites is responsible for high methanol synthesis activity. ZrO_2 modifies MoP in a way that significantly boosts the rate of methanol synthesis. Our in situ XAS and XRD results indicate the presence of a phase pure, crystalline MoP for unsupported nanoparticles after the pre-reduction treatment employed in both reactor and DRIFTS-TPSR tests. Together with the DRIFTS-TPSR results,

the resulting interpretation is that the rate of reaction of monodentate formate on MoP modified by ZrO_2 is greatly enhanced compared to MoP on a support lacking such strong interaction. Hence, the present work not only provides further evidence that stabilizing monodentate formate on MoP is an effective means to synthesize methanol, but it also shows that the reactivity of this intermediate can be enhanced by creating interfaces that strengthen its binding.

Table 2. Surface species and their assignments to TPSR-DRIFTS spectra.

| Peak Position (MoP/ZrO$_2$)	Peak Position (ZrO$_2$)	Assignment	Surface Species	References
1625 cm^{-1}	1620 cm^{-1}	$\nu_a(CO_3)$	bicarbonate	
1426 cm^{-1}	1419 cm^{-1}	$\nu_s(CO_3)$	bicarbonate	[72,76,85,86]
1221 cm^{-1}	1221 cm^{-1}	$\delta(OH)$	bicarbonate	
1581 cm^{-1}	1568 cm^{-1}	$\nu_a(CO_2)$	formate	
1388 cm^{-1}	1386 cm^{-1}	$\delta(CH)$	formate	[66,72,76,85,86]
1357 cm^{-1}	1359 cm^{-1}	$\nu_s(CO_2)$	formate	
1521 cm^{-1}	1528 cm^{-1}	$\nu_a(CO_3)$	bidentate carbonate	
1335 cm^{-1}	1321 cm^{-1}	$\nu_s(CO_3)$	bidentate carbonate	[76,85,86]
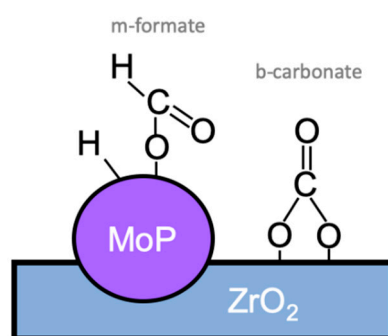
Figure 7. Schematic of surface species observed on MoP/ZrO$_2$ that are proposed to be responsible for its superior activity for methanol synthesis.

3. Experimental

3.1. Catalyst Synthesis

MoP nanoparticles were synthesized using the colloidal synthesis method described in a prior study [17]. Briefly, 7 mL Squalane (98% $C_{30}H_{62}$) and 3 mL trioctyl phosphine (90% $P(C_8H_{16})_3$) were mixed in a 50 mL round bottom flask at 200 rpm. The solution was heated under vacuum for 20 min at 120 °C to remove water. The solution was cooled under Argon atmosphere. When temperature reached below 60 °C, 1 mmol molybdenum hexacarbonyl was added to the flask. The solution was heated to 320 °C and held at this temperature for 2 h. A black suspension was observed after this procedure. Once the mixture cooled to room temperature, it was divided into two centrifuge tubes to recover the nanoparticles. Five milliliter hexanes and 15 mL ethanol were added to each centrifuge tube. The mixtures were sonicated for 5 min and centrifuged at 12,000 rpm for 3 min. The recovery protocol was performed a total of 3 times, and the recovered nanoparticles were re-dispersed in hexanes by sonication (30 min).

Commercially obtained catalyst supports, amorphous SiO_2 (Grace Davison, Columbia, ML, USA), γ-Al_2O_3 (Strem Chemicals, Boston, MA, USA), ZnO (Alfa Aesar, Harefreer, MA, USA), monoclinic ZrO_2 (Alfa Aesar), TiO_2 (Evonik, Essen, Missouri, Germany), and CeO_2 (Sigma Aldrich, St. Louis, Missouri, Germany) were calcined in air at 500 °C for 4 h. Nanoparticles were dispersed on various supports by adding 0.2–1 g of support to the

nanoparticle/hexanes suspension slowly until the suspension visibly segregated into solid and clear liquid components, indicating uptake of nanoparticles by the porous supports. The mixture was then sonicated for 2 h and centrifuged at 12,000 rpm for 3 min. The supernatant was discarded, and the precipitate was dried in air overnight.

3.2. Catalytic Testing

All catalysts were tested in a high pressure stainless steel flow reactor. Products were analyzed using an Agilent GC-MS equipped with mass spectrometer (MS), flame ionization detector (FID), and thermal conductivity detector (TCD), DB-624, DB 1, PLOT Q, HayeSepQ, and Shin Carbon columns. Two hundred and fifty milligrams of catalyst were typically used. Two percent argon mixed into the hydrogen feed was used as internal standard. Activity testing for CO_2 hydrogenation was performed at 40 bar and 250 °C. Differential conditions can be assumed in all tests as CO_2 conversions remained below 10%. Weight hourly space velocity (*WHSV*) was 10.8 h^{-1} in CO_2 hydrogenation experiments and was calculated using the following formula:

$$WHSV = \frac{Mass\ feed\ rate\ \left(\frac{g}{h}\right)}{Mass\ of\ catalyst\ (g)}.$$

Catalysts were reduced in situ at 450 °C in flowing hydrogen for 1 h prior to each test to remove the ligand trioctyl phosphine from the surface, as described in the prior work detailing the colloidal synthesis technique used in this study [17]. Activity data were collected after 7 h on stream for each catalyst. Argon was used as internal standard, and the flow rate of each species leaving the reactor was calculated as follows, where N_i is the molar flow rate of species i, $[i]$ and $[Ar]$ are the measured gas phase concentrations of species i and Argon, respectively, and N_{Ar} is the molar flow rate of Argon, which remains unchanged at the inlet and exit of the reactor:

$$N_i = \frac{[i]}{[Ar]} \times N_{Ar}.$$

The rate of methanol formation was calculated by normalizing the flow rate of methanol by the amount of Mo in the catalyst sample.

Conversion (X_{CO_2}) was calculated as follows from quantification of molar species of carbon containing products in the gas phase, and mass spectrometry confirmed the absence of any other species than those quantified.

$$X_{CO_2} = \frac{\sum N_i}{(\sum N_i) + N_{CO_2}},$$

where N_i is the flow rate of product species i, and N_{CO_2} is the flow rate of CO_2 in the reactor effluent.

Selectivity (S_i) for each species i was calculated by dividing the molar flow rate of each species by the flow rate of all carbon containing products at the exit of the reactor:

$$S_i = \frac{N_i}{\sum N_i}.$$

3.3. Catalyst Characterization

Transmission electron microscopy (TEM) was performed on an FEI Tecnai G2 F20 X-TWIN operated at a 200 kV accelerating voltage. TEM samples were prepared in air by suspending powder catalyst particles in methanol, sonicating for 15 min, and drop-casting them onto carbon-coated gold grids. Particle size analysis was performed on as synthesized MoP nanoparticles by averaging diameters of 163 particles.

Elemental analysis was performed on supported catalysts using Inductively Coupled Plasma-Mass Spectrometry (ICP-MS) after digestion of samples in aqua regia.

The oxidation state of catalyst powders were studied using X-ray Photoelectron Spectroscopy (XPS, PHI 5000 VersaProbe,) with Al K_α 1486.6 eV radiation. All spectra were calibrated to the line position of adventitious carbon at 284.8 eV.

In situ X-ray Diffraction (XRD) and X-ray Absorption Spectroscopy (XAS) at the Mo K-edge was performed at the European Synchrotron Radiation Facility (ESRF) at the Swiss-Norwegian Beamline (SNBL) BM31. Catalyst sample (3.9 mg) was fixed between two quartz wool plugs in a quartz capillary of 1 mm internal diameter and 0.2 mm wall thickness. The capillary was then mounted in a custom cell [87] and leak tested before operando experiments. XRD data were collected with a 2D detector using a Debye-Scherrer geometry and a wavelength of 0.049512 nm. Lanthanum Hexaboride powder (LaB_6) Standard Reference Material 660 c from the National Institute of Standards and Technology (NIST) was used for calibration. The XAS measurements were collected in transition mode using a Mo foil as reference for the XAS. XAS spectra were collected at the Mo K-edge during in situ activation at atmospheric pressure. XANES spectra were collected from 50 °C up to 700 °C with a 10 °C/min ramp rate, and each spectrum was collected in a range of 20 °C. The sample was held at 450 °C and 700 °C for 3 scans before collecting the EXAFS spectra. Between 3 and 6 X-ray energy sweeps were averaged to obtain a good signal to noise ratio. ATHENA and ARTEMIS software were used for the data treatment and fitting [88]. Fitting of the EXAFS spectra was generally performed in the 3–13 $Å^{-1}$ k-range and R-range 1–3.3. For the fitting process, the reduction amplitude factor (S_0^2) was extracted from a MoP standard, while the energy shift ($\Delta E0$) and the distance (R), and the coordination number (CN) of the Debye-Waller factor (σ^2) of each scattering path were refined. FEFF 9 was used to simulate the XANES spectrum at the P K edge (SCF = 6 A and FMS = 8 A) from MoP crystallographic structure (ICSD 186874: space group: P-6m2: a = b = 3.2500 Å; α = β = 90 γ = 120).

Ex situ P K-edge XANES data were collected on beamline 14-3 at the Stanford Synchrotron Radiation Lightsource (SSRL) in the fluorescence mode. Air-exposed samples were diluted to 1 wt % P in boron nitride to avoid significant self-absorption phenomena, and data were collected in the fluorescence mode using a four-element SSD (Vortex) inside a He-filled chamber to avoid X-ray attenuation by air. At least four scan sweeps were averaged together before data normalization. Data were analyzed using the Demeter software package [88]. After averaging several scan sweeps, a linear pre-edge was subtracted, and the data were normalized by the edge jump. A background, approximated with a spline function, was subtracted from the data to isolate $\chi(k)$ that was k^3-weighted prior to FT. The coordination numbers (*N*), the distance to the scattering atoms (*R*), and the mean-squared displacement (σ^2) were obtained by nonlinear fitting with least-squares refinement to the EXAFS equation of the FT data in q-space.

Diffuse Reflectance Fourier Transform Infrared Spectroscopy (DRIFTS) was performed on a Bruker Vertex 70 spectrometer with a liquid nitrogen-cooled HgCdTe (MCT) detector. Samples were loaded into a Praying Mantis DRIFTS chamber (Harrick) equipped with a water-cooled, high pressure and temperature reaction cell with ZnSe windows. The chamber pressure was controlled using a backpressure regulator. The chamber was purged with N_2 gas, and the catalyst was subsequently reduced in flowing H_2 at 450 °C for 1 h prior to measurement atmospheric pressure. The sample was brought to ambient temperature and pressurized in a 3/1 H_2/CO_2 mixture to 8.9 bar. Measurements were taken at 2 min intervals while ramping (10 °C/min) to 250 °C and 8.9 bar pressure in flowing H_2/CO_2 at 3:1 ratio. Conditions were held at 250 °C and 8.9 bar for 30 min. The DRIFTS cell was then purged with vacuum and re-pressurized in hydrogen to 8.9 bar to detect the hydrogenation of surface species. The complete DRIFTS data set for the TPSR experiments can be found in the SI (Figures S8 and S9).

4. Conclusions

Herein, we show that phase-pure MoP can reliably be synthesized using a colloidal synthesis method regardless of support, which is a significant improvement over the

common impregnation-TPR techniques for metal phosphide synthesis. The crystallinity of the initially amorphous MoP nanoparticles can be adjusted using high temperature reduction methods. The MoP phase catalyses the reduction of CO_2 to methanol and CO regardless of the support used. The rates of two competing reactions, methanol synthesis and reverse water gas shift, can be controlled by changing the support, and the relative rates determine selectivity. A striking manifestation of this is in the activity of MoP/ZrO_2, which is superior to all other catalysts in this study (at a CO_2 conversion of 1.4%) and demonstrates high selectivity to methanol (55.4%). DRIFTS-TPSR studies reveal that the formate binding on MoP/ZrO_2 is modified due to support effects of ZrO_2. The present work highlights the power of combining a systematic nanoparticle synthesis strategy with in situ characterisation of working catalysts in determining key factors controlling selectivity. Such approaches are essential tools for catalyst discovery at a time when we must synthesize fuels and chemicals with ever decreasing carbon footprints.

Supplementary Materials: The following are available online at https://www.mdpi.com/2073-4344/11/1/143/s1: Figure S1: C-H stretching region of the ex-situ IR spectra for supported MoP catalysts with the highest and lowest loading of MoP, showing the removal of ligands after hydrogen reduction treatment (450 °C, 1 hour); Table S1: Curve-fit results for the EXAFS data for Mo K-edge; Figure S2: XANES difference between crystalline MoP and as-prepared colloidal nanoparticles; Figure S3: First derivative of the XANES region of the Mo K-edge for different standards and as prepared Mo NPs at room temperature.; Figure S4: comparison of the FT of EXAFS signal at Mo K-edge for silica supported and unsupported Mo NPs; Table S2: Surface area (reported by manufacturer), Mo and P loadings determined via ICP and Mo/P ratios for amorphous MoP nanoparticles on various metal oxide supports; Figure S5: Conversion and methanol selectivity of MoP nanoparticle catalysts on various supports during CO_2 hydrogenation; Figure S6: X-ray Photoelectron Spectroscopy (XPS) of air exposed unsupported and zirconia supported MoP nanoparticles; Figure S7: Activity of ZrO_2 support during CO_2 hydrogenation. Figure S8: TPSR-DRIFTS full spectrum for MoP/ZrO_2; Figure S9: TPSR-DRIFTS full spectrum for ZrO_2; Figure S10: TPSR-DRIFTS C-H region.

Author Contributions: Conceptualization, M.S.D., A.G., M.R., T.F.J.; Methodology, M.S.D., A.G., M.R., J.M., J.A.S., S.K.R., E.V., J.L.S.; Formal Analysis, M.S.D., A.G., S.K.R., J.A.S.; Investigation, M.S.D., A.G., S.F.B., M.R.,T.F.J.; Resources, M.R., S.F.B., T.F.J.; Data Curation, M.S.D.; Writing—Original Draft Preparation, M.S.D., A.G.; Writing—Review & Editing, S.K.R., J.L.S., J.A.S., E.V., J.M., S.F.B., M.R., T.F.J.; Visualization, M.S.D., A.G., S.K.R., J.A.S.; Supervision, S.F.B., M.R., T.F.J.; Funding Acquisition, S.F.B., M.R., T.F.J. All authors have read and agreed to the published version of the manuscript.

Institutional Review Board Statement: Not applicable.

Informed Consent Statement: Not applicable.

Conflicts of Interest: The authors declare no conflict of interest.

References

1. Friedlingstein, P.; Andrew, R.M.; Rogelj, J.; Peters, G.P.; Canadell, J.G.; Knutti, R.; Luderer, G.; Raupach, M.R.; Schaeffer, M.; van Vuuren, D.P. Persistent growth of CO_2 emissions and implications for reaching climate targets. *Nat. Geosci.* **2014**, *7*, 709–715. [CrossRef]
2. Porosoff, M.D.; Yan, B.; Chen, J.G. Catalytic reduction of CO_2 by H 2 for synthesis of CO, methanol and hydrocarbons: Challenges and opportunities. *Energy Environ. Sci.* **2016**, *9*, 62–73. [CrossRef]
3. Scott, V.; Gilfillan, S.; Markusson, N.; Chalmers, H.; Haszeldine, R.S. Last chance for carbon capture and storage. *Nat. Clim. Chang.* **2013**, *3*, 105–111. [CrossRef]
4. Haszeldine, R.S. Carbon capture and storage: How green can black be? *Science* **2009**, *325*, 1647–1652. [CrossRef] [PubMed]
5. Jiang, X.; Nie, X.; Guo, X.; Song, C.; Chen, J.G. Recent Advances in Carbon Dioxide Hydrogenation to Methanol via Heterogeneous Catalysis. *Chem. Rev.* **2020**, *120*, 7984–8034. [CrossRef]
6. Martin, O.; Martín, A.J.; Mondelli, C.; Mitchell, S.; Segawa, T.F.; Hauert, R.; Drouilly, C.; Curulla-Ferré, D.; Pérez-Ramírez, J. Indium oxide as a superior catalyst for methanol synthesis by CO_2 hydrogenation. *Angew. Chem. Int. Ed.* **2016**, *55*, 6261–6265. [CrossRef]
7. Frei, M.S.; Mondelli, C.; García-Muelas, R.; Kley, K.S.; Puértolas, B.; López, N.; Safonova, O.V.; Stewart, J.A.; Ferré, D.C.; Pérez-Ramírez, J. Atomic-scale engineering of indium oxide promotion by palladium for methanol production via CO_2 hydrogenation. *Nat. Commun.* **2019**, *10*, 1–11. [CrossRef]
8. Snider, J.L.; Streibel, V.; Hubert, M.A.; Choksi, T.S.; Valle, E.; Upham, D.C.; Schumann, J.; Duyar, M.S.; Gallo, A.; Abild-Pedersen, F. Revealing the synergy between oxide and alloy phases on the performance of bimetallic In–Pd catalysts for CO_2 hydrogenation to methanol. *ACS Catal.* **2019**, *9*, 3399–3412. [CrossRef]
9. Studt, F.; Sharafutdinov, I.; Abild-Pedersen, F.; Elkjær, C.F.; Hummelshøj, J.S.; Dahl, S.; Chorkendorff, I.; Nørskov, J.K. Discovery of a Ni-Ga catalyst for carbon dioxide reduction to methanol. *Nat. Chem.* **2014**, *6*, 320–324. [CrossRef]
10. Gallo, A.; Snider, J.L.; Sokaras, D.; Nordlund, D.; Kroll, T.; Ogasawara, H.; Kovarik, L.; Duyar, M.S.; Jaramillo, T.F. Ni_5Ga_3 catalysts for CO_2 reduction to methanol: Exploring the role of Ga surface oxidation/reduction on catalytic activity. *Appl. Catal. B Environ.* **2020**, *267*, 118369. [CrossRef]
11. Duyar, M.S.; Gallo, A.; Snider, J.L.; Jaramillo, T.F. Low-pressure methanol synthesis from CO_2 over metal-promoted Ni-Ga intermetallic catalysts. *J. CO_2 Util.* **2020**, *39*, 101151. [CrossRef]
12. Duyar, M.S.; Tsai, C.; Snider, J.L.; Singh, J.A.; Gallo, A.; Yoo, J.S.; Medford, A.J.; Abild-Pedersen, F.; Studt, F.; Kibsgaard, J. A highly active molybdenum phosphide catalyst for methanol synthesis from CO and CO_2. *Angew. Chem. Int. Ed.* **2018**, *57*, 15045–15050. [CrossRef] [PubMed]
13. Olah, G.A. After oil and gas: Methanol economy. *Catal. Lett.* **2004**, *93*, 1–2. [CrossRef]
14. Olah, G.A.; Goeppert, A.; Prakash, G.S. *Beyond Oil and Gas: The Methanol Economy*; John Wiley & Sons: Hoboken, NJ, USA, 2011.
15. Simon Araya, S.; Liso, V.; Cui, X.; Li, N.; Zhu, J.; Sahlin, S.L.; Jensen, S.H.; Nielsen, M.P.; Kær, S.K. A Review of The Methanol Economy: The Fuel Cell Route. *Energies* **2020**, *13*, 596. [CrossRef]
16. Dalena, F.; Senatore, A.; Basile, M.; Knani, S.; Basile, A.; Iulianelli, A. Advances in Methanol Production and Utilization, with Particular Emphasis toward Hydrogen Generation via Membrane Reactor Technology. *Membranes* **2018**, *8*, 98. [CrossRef] [PubMed]
17. McEnaney, J.M.; Crompton, J.C.; Callejas, J.F.; Popczun, E.J.; Biacchi, A.J.; Lewis, N.S.; Schaak, R.E. Amorphous molybdenum phosphide nanoparticles for electrocatalytic hydrogen evolution. *Chem. Mater.* **2014**, *26*, 4826–4831. [CrossRef]
18. Surisetty, V.R.; Tavasoli, A.; Dalai, A. Synthesis of higher alcohols from syngas over alkali promoted MoS_2 catalysts supported on multi-walled carbon nanotubes. *Appl. Catal. A Gen.* **2009**, *365*, 243–251. [CrossRef]
19. Woo, H.C.; Nam, I.S.; Lee, J.S.; Chung, J.S.; Kim, Y.G. Structure and Distribution of Alkali Promoter in K/MoS_2 Catalysts and Their Effects on Alcohol Synthesis from Syngas. *J. Catal.* **1993**, *142*, 672–690. [CrossRef]
20. Iranmahboob, J.; Hill, D.O. Alcohol synthesis from syngas over K_2CO_3/CoS/MoS_2 on activated carbon. *Catal. Lett.* **2002**, *78*, 49–55. [CrossRef]
21. Santos, V.P.; van der Linden, B.; Chojecki, A.; Budroni, G.; Corthals, S.; Shibata, H.; Meima, G.R.; Kapteijn, F.; Makkee, M.; Gascon, J. Mechanistic insight into the synthesis of higher alcohols from syngas: The role of K promotion on MoS_2 catalysts. *ACS Catal.* **2013**, *3*, 1634–1637. [CrossRef]
22. Morrill, M.R.; Thao, N.T.; Shou, H.; Davis, R.J.; Barton, D.G.; Ferrari, D.; Agrawal, P.K.; Jones, C.W. Origins of unusual alcohol selectivities over mixed MgAl oxide-supported K/MoS_2 catalysts for higher alcohol synthesis from syngas. *ACS Catal.* **2013**, *3*, 1665–1675. [CrossRef]
23. Iranmahboob, J.; Hill, D.O.; Toghiani, H. K_2CO_3/Co-MoS_2/clay catalyst for synthesis of alcohol: Influence of potassium and cobalt. *Appl. Catal. A Gen.* **2002**, *231*, 99–108. [CrossRef]
24. Ferrari, D.; Budroni, G.; Bisson, L.; Rane, N.; Dickie, B.; Kang, J.; Rozeveld, S. Effect of potassium addition method on MoS_2 performance for the syngas to alcohol reaction. *Appl. Catal. A Gen.* **2013**, *462*, 302–309. [CrossRef]
25. Iranmahboob, J.; Toghiani, H.; Hill, D.O. Dispersion of alkali on the surface of Co-MoS_2/clay catalyst: A comparison of K and Cs as a promoter for synthesis of alcohol. *Appl. Catal. A Gen.* **2003**, *247*, 207–218. [CrossRef]
26. Xiao, H.; Li, D.; Li, W.; Sun, Y. Study of induction period over K_2CO_3/MoS_2 catalyst for higher alcohols synthesis. *Fuel Process. Technol.* **2010**, *91*, 383–387. [CrossRef]

27. Qi, H.; Li, D.; Yang, C.; Ma, Y.; Li, W.; Sun, Y.; Zhong, B. Nickel and manganese co-modified K/MoS$_2$ catalyst: High performance for higher alcohols synthesis from CO hydrogenation. *Catal. Commun.* **2003**, *4*, 339–342. [CrossRef]

28. Patterson, P.M.; Das, T.K.; Davis, B.H. Carbon monoxide hydrogenation over molybdenum and tungsten carbides. *Appl. Catal. A Gen.* **2003**, *251*, 449–455. [CrossRef]

29. Xiang, M.; Li, D.; Xiao, H.; Zhang, J.; Qi, H.; Li, W.; Zhong, B.; Sun, Y. Synthesis of higher alcohols from syngas over Fischer–Tropsch elements modified K/β-Mo$_2$C catalysts. *Fuel* **2008**, *87*, 599–603. [CrossRef]

30. Xiang, M.; Li, D.; Li, W.; Zhong, B.; Sun, Y. Synthesis of higher alcohols from syngas over K/Co/β-Mo$_2$C catalysts. *Catal. Commun.* **2007**, *8*, 503–507. [CrossRef]

31. Park, K.Y.; Seo, W.K.; Lee, J.S. Selective synthesis of light olefins from syngas over potassium-promoted molybdenum carbide catalysts. *Catal. Lett.* **1991**, *11*, 349–356. [CrossRef]

32. Zaman, S.F.; Smith, K.J. Synthesis gas conversion over MoP catalysts. *Catal. Commun.* **2009**, *10*, 468–471. [CrossRef]

33. Zaman, S.F.; Smith, K.J. A study of K-promoted MoP–SiO$_2$ catalysts for synthesis gas conversion. *Appl. Catal. A Gen.* **2010**, *378*, 59–68. [CrossRef]

34. Zaman, S.F.; Smith, K.J. Synthesis gas conversion over a Rh–K–MoP/SiO$_2$ catalyst. *Catal. Today* **2011**, *171*, 266–274. [CrossRef]

35. Ten Have, I.C.; Valle, E.; Gallo, A.; Snider, J.L.; Duyar, M.S.; Jaramillo, T.F. Development of Molybdenum Phosphide Catalysts for Higher Alcohol Synthesis from Syngas by Exploiting Support and Promoter Effects. *Energy Technol.* **2019**, *7*, 1801102. [CrossRef]

36. Wang, S.; Ge, H.; Sun, S.; Zhang, J.; Liu, F.; Wen, X.; Yu, X.; Wang, L.; Zhang, Y.; Xu, H. A new molybdenum nitride catalyst with rhombohedral MoS$_2$ structure for hydrogenation applications. *J. Am. Chem. Soc.* **2015**, *137*, 4815–4822. [CrossRef]

37. Zaman, S.F.; Pasupulety, N.; Al-Zahrani, A.A.; Daous, M.A.; Al-Shahrani, S.S.; Driss, H.; Petrov, L.A.; Smith, K.J. Carbon monoxide hydrogenation on potassium promoted Mo$_2$N catalysts. *Appl. Catal. A Gen.* **2017**, *532*, 133–145. [CrossRef]

38. Liu, P.; Rodriguez, J.A. Catalytic properties of molybdenum carbide, nitride and phosphide: A theoretical study. *Catal. Lett.* **2003**, *91*, 247–252. [CrossRef]

39. Pistonesi, C.; Pronsato, M.E.; Bugyi, L.S.; Juan, A. Theoretical model for CO adsorption and dissociation on clean and K-doped β-Mo$_2$C surfaces. *J. Phys. Chem. C* **2012**, *116*, 24573–24581. [CrossRef]

40. Medford, A.J.; Vojvodic, A.; Studt, F.; Abild-Pedersen, F.; Nørskov, J.K. Elementary steps of syngas reactions on Mo$_2$C (0 0 1): Adsorption thermochemistry and bond dissociation. *J. Catal.* **2012**, *290*, 108–117. [CrossRef]

41. Wu, Z.; Sun, F.; Wu, W.; Feng, Z.; Liang, C.; Wei, Z.; Li, C. On the surface sites of MoP/SiO$_2$ catalyst under sulfiding conditions: IR spectroscopy and catalytic reactivity studies. *J. Cataly.* **2004**, *222*, 41–52. [CrossRef]

42. Porosoff, M.D.; Baldwin, J.W.; Peng, X.; Mpourmpakis, G.; Willauer, H.D. Potassium-Promoted Molybdenum Carbide as a Highly Active and Selective Catalyst for CO$_2$ Conversion to CO. *ChemSusChem* **2017**, *10*, 2408–2415. [CrossRef] [PubMed]

43. Tominaga, H.; Nagai, M. Density functional study of carbon dioxide hydrogenation on molybdenum carbide and metal. *Appl. Cataly. A Gen.* **2005**, *282*, 5–13. [CrossRef]

44. Kunkel, C.; Viñes, F.; Ramírez, P.J.; Rodriguez, J.A.; Illas, F. Combining Theory and Experiment for Multitechnique Characterization of Activated CO$_2$ on Transition Metal Carbide (001) Surfaces. *J. Phys. Chem. C* **2018**, *123*, 7567–7576. [CrossRef]

45. Rui, N.; Wang, Z.; Sun, K.; Ye, J.; Ge, Q.; Liu, C.-J. CO$_2$ hydrogenation to methanol over Pd/In$_2$O$_3$: Effects of Pd and oxygen vacancy. *Appl. Cataly. B Environ.* **2017**, *218* (Suppl. C), 488–497. [CrossRef]

46. Geng, W.; Han, H.; Liu, F.; Liu, X.; Xiao, L.; Wu, W. N,P,S-codoped C@nano-Mo$_2$C as an efficient catalyst for high selective synthesis of methanol from CO$_2$ hydrogenation. *J. CO$_2$ Util.* **2017**, *21*, 64–71. [CrossRef]

47. Chen, Y.; Choi, S.; Thompson, L.T. Low temperature CO$_2$ hydrogenation to alcohols and hydrocarbons over Mo$_2$C supported metal catalysts. *J. Catal.* **2016**, *343*, 147–156. [CrossRef]

48. Li, T.; Virginie, M.; Khodakov, A.Y. Effect of potassium promotion on the structure and performance of alumina supported carburized molybdenum catalysts for Fischer-Tropsch synthesis. *Appl. Catal. A Gen.* **2017**, *542*, 154–162. [CrossRef]

49. Chan, K.; Tsai, C.; Hansen, H.A.; Nørskov, J.K. Molybdenum sulfides and selenides as possible electrocatalysts for CO$_2$ reduction. *ChemCatChem* **2014**, *6*, 1899–1905. [CrossRef]

50. Hong, X.; Chan, K.; Tsai, C.; Nørskov, J.K. How doped MoS$_2$ breaks transition-metal scaling relations for CO$_2$ electrochemical reduction. *ACS Catal.* **2016**, *6*, 4428–4437. [CrossRef]

51. Peng, H.; Lu, J.; Wu, C.; Yang, Z.; Chen, H.; Song, W.; Li, P.; Yin, H. Co-doped MoS$_2$ NPs with matched energy band and low overpotential high efficiently convert CO$_2$ to methanol. *Appl. Surf. Sci.* **2015**, *353*, 1003–1012. [CrossRef]

52. Fields, M.; Tsai, C.; Chen, L.D.; Abild-Pedersen, F.; Nørskov, J.K.; Chan, K. Scaling Relations for Adsorption Energies on Doped Molybdenum Phosphide Surfaces. *ACS Catal.* **2017**, *7*, 2528–2534. [CrossRef]

53. Sun, X.; Lu, L.; Wu, C.; Yang, D.; Chen, C.; Han, B. MoP Nanoparticles Supported on In-doped Porous Carbon: Outstanding Catalysts for High-efficient CO$_2$ Electroreduction. *Angew. Chem. Int. Ed.* **2018**, *57*, 2427–2431. [CrossRef] [PubMed]

54. Saito, M.; Anderson, R.B. The activity of several molybdenum compounds for the methanation of CO$_2$. *J. Catal.* **1981**, *67*, 296–302. [CrossRef]

55. Studt, F.; Behrens, M.; Kunkes, E.L.; Thomas, N.; Zander, S.; Tarasov, A.; Schumann, J.; Frei, E.; Varley, J.B.; Abild-Pedersen, F.; et al. The Mechanism of CO and CO$_2$ Hydrogenation to Methanol over Cu-Based Catalysts. *ChemCatChem* **2015**, *7*, 1105–1111. [CrossRef]

56. Clark, P.A.; Oyama, S.T. Alumina-supported molybdenum phosphide hydroprocessing catalysts. *J. Catal.* **2003**, *218*, 78–87. [CrossRef]

57. Oyama, S.; Clark, P.; Teixeira da Silva, V.; Lede, E.; Requejo, F. XAFS characterization of highly active alumina-supported molybdenum phosphide catalysts (MoP/Al2O3) for hydrotreating. *J. Phys. Chem. B* **2001**, *105*, 4961–4966. [CrossRef]

58. Wang, X.; Clark, P.; Oyama, S.T. Synthesis, Characterization, and Hydrotreating Activity of Several Iron Group Transition Metal Phosphides. *J. Catal.* **2002**, *208*, 321–331. [CrossRef]

59. Yang, S.; Chen, G.; Ricciardulli, A.G.; Zhang, P.; Zhang, Z.; Shi, H.; Ma, J.; Zhang, J.; Blom, P.; Feng, X. Topochemical Synthesis of Two-Dimensional Transition Metal Phosphides Using Phosphorene Templates. *Angew. Chem. Int. Edition* **2020**, *59*, 465–470. [CrossRef]

60. Shi, Y.; Zhang, B. Recent advances in transition metal phosphide nanomaterials: Synthesis and applications in hydrogen evolution reaction. *Chem. Soc. Rev.* **2016**, *45*, 1529–1541. [CrossRef]

61. Kattel, S.; Yan, B.; Yang, Y.; Chen, J.G.; Liu, P. Optimizing Binding Energies of Key Intermediates for CO_2 Hydrogenation to Methanol over Oxide-Supported Copper. *J. Am. Chem.Soc.* **2016**, *138*, 12440–12450. [CrossRef]

62. Blanchard, P.; Grosvenor, A.; Cavell, R.; Mar, A. X-ray Photoelectron and Absorption Spectroscopy of Metal-Rich Phosphides M2P and M3P (M = Cr-Ni). *Chem. Mater.* **2008**, *20*, 7081–7088. [CrossRef]

63. Tan, Y.; Sun, D.; Yu, H.; Jiao, S.; Gong, Y.; Yan, S.; Chen, Z.; Xing, X.; Mo, G.; Cai, Q.; et al. In Situ Time-Resolved X-ray Absorption Fine Structure and Small Angle X-ray Scattering Revealed an Unexpected Phase Structure Transformation during the Growth of Nickel Phosphide Nanoparticles. *J. Phys. Chem. C* **2018**, *122*, 16397–16405. [CrossRef]

64. Prinetto, F.; Cerrato, G.; Ghiotti, G.; Chiorino, A.; Campa, M.C.; Gazzoli, D.; Indovina, V. Formation of the MoVI Surface Phase on MoOx/ZrO2 Catalysts. *J. Phys. Chem.* **1995**, *99*, 5556–5567. [CrossRef]

65. Stangeland, K.; Li, H.; Yu, Z. Thermodynamic Analysis of Chemical and Phase Equilibria in CO_2 Hydrogenation to Methanol, Dimethyl Ether, and Higher Alcohols. *Ind. Eng. Chem. Res.* **2018**, *57*, 4081–4094. [CrossRef]

66. Larmier, K.; Liao, W.C.; Tada, S.; Lam, E.; Verel, R.; Bansode, A.; Urakawa, A.; Comas-Vives, A.; Copéret, C. CO_2-to-Methanol Hydrogenation on Zirconia-Supported Copper Nanoparticles: Reaction Intermediates and the Role of the Metal–Support Interface. *Angew. Chem. Int. Ed.* **2017**, *56*, 2318–2323. [CrossRef] [PubMed]

67. Li, K.; Chen, J.G. CO_2 Hydrogenation to Methanol over ZrO2-Containing Catalysts: Insights into ZrO2 Induced Synergy. *ACS Catal.* **2019**, *9*, 7840–7861. [CrossRef]

68. Wang, W.; Wang, S.; Ma, X.; Gong, J. Recent advances in catalytic hydrogenation of carbon dioxide. *Chem. Soc. Rev.* **2011**, *40*, 3703–3727. [CrossRef]

69. Słoczyński, J.; Grabowski, R.; Olszewski, P.; Kozłowska, A.; Stoch, J.; Lachowska, M.; Skrzypek, J. Effect of metal oxide additives on the activity and stability of Cu/ZnO/ZrO2 catalysts in the synthesis of methanol from CO_2 and H_2. *Appl. Catal. A Gen.* **2006**, *310*, 127–137. [CrossRef]

70. Arena, F.; Barbera, K.; Italiano, G.; Bonura, G.; Spadaro, L.; Frusteri, F. Synthesis, characterization and activity pattern of Cu–ZnO/ZrO2 catalysts in the hydrogenation of carbon dioxide to methanol. *J. Catal.* **2007**, *249*, 185–194. [CrossRef]

71. Schilke, T.C.; Fisher, I.A.; Bell, A.T. In SituInfrared Study of Methanol Synthesis from CO_2/H_2on Titania and Zirconia Promoted Cu/SiO2. *J. Catal.* **1999**, *184*, 144–156. [CrossRef]

72. Fisher, I.; Bell, A. In-situ infrared study of methanol synthesis from H_2/CO_2 over Cu/SiO2 and Cu/ZrO2/SiO2. *J. Catal.* **1997**, *172*, 222–237. [CrossRef]

73. Jung, K.-D.; Bell, A.T. Role of hydrogen spillover in methanol synthesis over Cu/ZrO2. *J. Catal.* **2000**, *193*, 207–223. [CrossRef]

74. Gao, P.; Li, F.; Zhan, H.; Zhao, N.; Xiao, F.; Wei, W.; Zhong, L.; Wang, H.; Sun, Y. Influence of Zr on the performance of Cu/Zn/Al/Zr catalysts via hydrotalcite-like precursors for CO_2 hydrogenation to methanol. *J. Catal.* **2013**, *298*, 51–60. [CrossRef]

75. Wang, J.; Li, G.; Li, Z.; Tang, C.; Feng, Z.; An, H.; Liu, H.; Liu, T.; Li, C. A highly selective and stable ZnO-ZrO2 solid solution catalyst for CO_2 hydrogenation to methanol. *Sci. Adv.* **2017**, *3*, e1701290. [CrossRef] [PubMed]

76. Solis-Garcia, A.; Louvier-Hernandez, J.F.; Almendarez-Camarillo, A.; Fierro-Gonzalez, J.C. Participation of surface bicarbonate, formate and methoxy species in the carbon dioxide methanation catalyzed by ZrO2-supported Ni. *Appl. Catal. B Environ.* **2017**, *218*, 611–620. [CrossRef]

77. Korhonen, S.T.; Bañares, M.A.; Fierro, J.L.G.; Krause, A.O.I. Adsorption of methanol as a probe for surface characteristics of zirconia-, alumina-, and zirconia/alumina-supported chromia catalysts. *Catal. Today* **2007**, *126*, 235–247. [CrossRef]

78. Lustemberg, P.G.; Bosco, M.V.; Bonivardi, A.; Busnengo, H.F.; Ganduglia-Pirovano, M. Insights into the nature of formate species in the decomposition and reaction of methanol over cerium oxide surfaces: A combined infrared spectroscopy and density functional theory study. *J. Phys. Chem. C* **2015**, *119*, 21452–21464. [CrossRef]

79. Busca, G.; Lorenzelli, V. Infrared spectroscopic identification of species arising from reactive adsorption of carbon oxides on metal oxide surfaces. *Mater. Chem.* **1982**, *7*, 89–126. [CrossRef]

80. Bandara, A.; Kubota, J.; Wada, A.; Domen, K.; Hirose, C. Adsorption and reactions of formic acid on (2 × 2)-NiO (111)/Ni (111) surface. 1. TPD and IRAS studies under ultrahigh vacuum conditions. *J. Phys. Chem.* **1996**, *100*, 14962–14968. [CrossRef]

81. Calatayud, M.; Collins, S.E.; Baltanás, M.A.; Bonivardi, A.L. Stability of formate species on β-Ga2 O3. *Phys. Chem. Chem. Phys.* **2009**, *11*, 1397–1405. [CrossRef]

82. Marwood, M.; Doepper, R.; Renken, A. In-situ surface and gas phase analysis for kinetic studies under transient conditions the catalytic hydrogenation of CO_2. *Appl. Catal. A Gen.* **1997**, *151*, 223–246. [CrossRef]

83. Li, C.; Domen, K.; Maruya, K.-I.; Onishi, T. Spectroscopic identification of adsorbed species derived from adsorption and decomposition of formic acid, methanol, and formaldehyde on cerium oxide. *J. Catal.* **1990**, *125*, 445–455. [CrossRef]

84. Binet, C.; Daturi, M.; Lavalley, J.-C. IR study of polycrystalline ceria properties in oxidised and reduced states. *Catal. Today* **1999**, *50*, 207–225. [CrossRef]

85. Daturi, M.; Binet, C.; Lavalley, J.; Blanchard, G. Surface FTIR investigations on CexZr1−xO$_2$ system. *Surf. Interface Anal. Int. J. Devot. Dev. Appl. Tech. Anal. Surf. Interfaces Thin Films* **2000**, *30*, 273–277. [CrossRef]

86. Takano, H.; Kirihata, Y.; Izumiya, K.; Kumagai, N.; Habazaki, H.; Hashimoto, K. Highly active Ni/Y-doped ZrO$_2$ catalysts for CO$_2$ methanation. *Appl. Surf. Sci.* **2016**, *388*, 653–663. [CrossRef]

87. Tsakoumis, N.E.; Voronov, A.; Rønning, M.; Beek, W.V.; Borg, Ø.; Rytter, E.; Holmen, A. Fischer–Tropsch synthesis: An XAS/XRPD combined in situ study from catalyst activation to deactivation. *J. Catal.* **2012**, *291*, 138–148. [CrossRef]

88. Ravel, B.; Newville, M. Athena, Artemis, Hephaestus: Data analysis for X-ray absorption spectroscopy using IFEFFIT. *J. Synchrotron Radiat.* **2005**, *12*, 537–541. [CrossRef]